Please cite this paper as follows:
Shin-Jang Sung, Li-Wei Liu, Hong-Ki Hong and Han-Chin Wu, Evolution of Yield Surface in the 2D and 3D Stress Spaces, International Journal of Solids and Structures, Vol.48, pp.1054-1069, 2011.

International Journal of Solids and Structures 48 (2011) 1054–1069

Contents lists available at ScienceDirect

International Journal of Solids and Structures

journal homepage: www.elsevier.com/locate/ijsolstr

Evolution of yield surface in the 2D and 3D stress spaces

Shin-Jang Sung [a], Li-Wei Liu [a], Hong-Ki Hong [a,*], Han-Chin Wu [a,b]

[a] Department of Civil Engineering, National Taiwan University, Taipei 10617, Taiwan
[b] Department of Civil and Environmental Engineering, University of Iowa, Iowa City, IA, USA

ARTICLE INFO

Article history:
Received 14 September 2010
Received in revised form 13 November 2010
Available online 22 December 2010

Keywords:
Yield surface
Yield surface rotation
Automated yield stress determination
Axial–torsional-internal pressure experiment

ABSTRACT

Initial and subsequent yield surfaces for 6061 aluminum, determined by a method of automated yield stress probing, are presented in the 2D ($\sigma_{zz} - \sigma_{\theta z}$) and 3D ($\sigma_{\theta\theta} - \sigma_{zz} - \sigma_{\theta z}$) stress spaces. In the ($\sigma_{zz} - \sigma_{\theta z}$) space, yield surfaces at small pre-strains show the noses and unapparent cross effect. At larger pre-strains, they become ellipses with positive cross effect. In the ($\sigma_{\theta\theta} - \sigma_{zz} - \sigma_{\theta z}$) space, the initial yield surface is not well described by von Mises yield criterion due to material anisotropy. The yield surfaces of various torsional pre-strains show obvious rotation around the σ_{zz} axis but they do not rotate when subjected to axial pre-strains. Therefore, the rotation behavior of yield surface is pre-strain path dependent. The rotation of yield surfaces in the 3D space is the emphasis of the present paper. Coupled axial–torsional behavior subjected to torsion after axial pre-strain are also presented for the same material that is used to determine the yield surfaces. This information is useful for verification of constitutive models.

1. Introduction

Evolution of yield surface is one of important characteristics of plastic behavior. Three main modes of yield surface evolution, including isotropic expansion or contraction, translation, and distortion, are well recognized by researchers. However, the rotation of yield surface has not been much investigated. The yield surfaces are influenced by many factors. The most obvious one is the difference in material, including different heat treatments. In addition, the initial anisotropy induced by the manufacturing process is quite important. The anisotropic materials show more complicated behavior under plastic deformation by inducing additional anisotropy. For small plastic pre-strains of less than 1%, experimental results showed no cross effect (Phillips and Tang, 1972; Phillips et al., 1974; Phillips and Moon, 1977; Moreton et al., 1978; Wu and Yeh, 1991). For plastic pre-strains larger than 1%, two different kinds of evolution of yield surfaces including expanding with positive cross effect and shrinking with negative cross effect were observed (Hecker, 1971; Helling et al., 1986; Khan et al., 2009, 2010a,b; Ng et al., 1979; Shiratori et al., 1973; Stout et al., 1985; Wu, 2003). There were also experimental results which showed contraction first and then expansion with increasing plastic pre-strains (Helling et al., 1986; Shiratori et al., 1973; Williams and Svensson, 1971). More information about the evolution of yield surface was reported in Ellis et al. (1983), Boucher et al. (1995), Lissenden and Lei (2004), and in the book (Wu, 2005).

The experimental study of the yield surface was generally conducted on plane stress specimens including plate-like specimens or thin-walled tubes. For rolled plates or cross-shaped specimens, tensile tests with different loading axes or biaxial testing were mostly used (Ikegami, 1975a,b; Kreissig and Schindler, 1986; Losilla and Tourabi, 2004). In thin-walled tubes with z denoting the axial direction and θ the circumferential direction, the traditional axial–torsional testing was limited to yield loci of the ($\sigma_{zz} - \sigma_{\theta z}$) space with zero hoop stress $\sigma_{\theta\theta}$, where σ_{zz} was the axial stress and $\sigma_{\theta z}$ was the shear stress. Additional internal or external pressure was needed to obtain stress states in the ($\sigma_{\theta\theta} - \sigma_{zz}$) space or in the ($\sigma_{\theta\theta} - \sigma_{zz} - \sigma_{\theta z}$) space. Probing subsequent yield surfaces in the half ($\sigma_{\theta\theta} - \sigma_{zz}$) space, only tension in the hoop stress, can be accomplished by simply applying axial load and internal pressure. These works were presented in Lipkin and Swearengen (1975), Phillips and Das (1985), Khan et al. (2010b). Applying additional external pressure was harder but needed to probe yield surfaces in the whole ($\sigma_{\theta\theta} - \sigma_{zz}$) space, including compression in hoop stress, and the works were reported by Shiratori et al. (1973) and Moreton et al. (1978). There have been only a few experimental results devoted to the determination of yield surface in the ($\sigma_{\theta\theta} - \sigma_{zz} - \sigma_{\theta z}$) space. Shiratori's group (Shiratori et al., 1973) investigated subsequent yield surfaces in the ($\sigma_{\theta\theta} - \sigma_{zz} - \sigma_{\theta z}$) space by plotting contour lines representing constant axial stresses or shear stresses in the ($\sigma_{zz} - \sigma_{\theta z}$) or ($\sigma_{\theta\theta} - \sigma_{zz}$) space, respectively. However, data points in that paper were insufficient to draw contour lines in detail. Phillips and Das (1985) determined initial and subsequent yield surfaces in the ($\sigma_{\theta\theta} - \sigma_{zz} - \sigma_{\theta z}$) space and presented yield loci of the yield ellipsoid cut by various planes parallel to the $\sigma_{\theta z}$ axis.

* Corresponding author. Fax: +886 2 27396752.
E-mail address: hkhong@ntu.edu.tw (H.-K. Hong).

0020-7683/$ - see front matter © 2010 Elsevier Ltd. All rights reserved.
doi:10.1016/j.ijsolstr.2010.12.011

A different type of experiment performed by Samanta's group (Kim, 1992; Kumar et al., 1991; Mallick et al., 1991) on thin-walled tubes was to independently control the axial load, torsion, and internal pressure to simulate uniaxial stressing of a thin-walled element along a direction making an angle α with the circumferential direction θ of the tube (called off-axis tension by Takeda and Mizukami (2008)). The uniaxial yield stress denoted by σ_u was determined and plotted against the changing α in Fig. 1 for three conditions of torsion pre-strain. Although not mentioned in their articles, these experimental results actually led to rotation of subsequent yield surfaces in the $(\sigma_{\theta\theta} - \sigma_{zz} - \sigma_{\theta z})$ space and the details about the rotation of yield surfaces will be discussed in Section 2. In Mallick et al. (1991), the yield surfaces evolved and axes of material orthotropy changed when subjected to torsion pre-strains. But, the yield surfaces were presented in the first quadrant of spaces formed by axes of orthotropy and the rotation of yield surface was not apparent in that presentation. Takeda investigated initial and subsequent anisotropy by use of off-axis torsion tests and off-axis tension tests and used the anisotropic yield function to describe the results in various materials (Takeda, 1991, 1993; Takeda and Chen, 2001; Takeda and Mizukami, 2008; Takeda and Nasu, 1991). His articles also revealed that anisotropy might exist in fully annealed (–O) specimens which had been subjected to deformation during manufacturing.

Until now, no systematic experimental results about anisotropic initial and subsequent yield surfaces in the $(\sigma_{\theta\theta} - \sigma_{zz} - \sigma_{\theta z})$ space have been reported in the literature. This information is important in mathematically modeling the plastic behavior of anisotropic materials. In the present study, initial yield surfaces were obtained in the $(\sigma_{\theta\theta} - \sigma_{zz} - \sigma_{\theta z})$ space, which indicated initial anisotropy of the material tested. After axial pre-strains or torsional pre-strains, subsequent yield surfaces were probed to illustrate the evolution of yield surfaces. Special attention was given to the rotation of yield surfaces. In addition, a set of experiments was conducted to determine the coupled axial–torsional behavior of thin-walled tubes subjected to various boundary conditions. The latter information is useful for the verification of constitutive models.

2. Rotation of subsequent yield surfaces

Mallick et al. (1991) conducted experiments on thin-walled tubes with axial force, torsion, and internal pressure independently controlled to simulate pure tension of a thin-walled element along a direction making an angle α with the circumferential direction θ of the tube. The axial direction of the tube is denoted by z. The uniaxial tensile stress increased monotonically and the yield stress σ_u was determined for each value of α. Thus, σ_u vs. α curves were plotted and shown in Fig. 1 for three kinds of specimens: (1) as-received; (2) specimens subjected to torsional pre-strains of $\gamma = 0.1$; and (3) specimens subjected to torsional pre-strains of $\gamma = 0.3$.

The yield stress σ_u can be transformed into a set of stress components $(\sigma_{\theta\theta}, \sigma_{zz}, \sigma_{\theta z})$ by use of

$$\sigma_{\theta\theta} = \sigma_u \cos^2 \alpha, \quad \sigma_{zz} = \sigma_u \sin^2 \alpha, \quad \sigma_{\theta z} = \sigma_u \sin \alpha \cos \alpha. \tag{1}$$

Using these stress components a point can be plotted in the $(\sigma_{\theta\theta} - \sigma_{zz} - \sigma_{\theta z})$ space, with $\sigma_{\theta\theta}$ and σ_{zz} forming the biaxial plane,

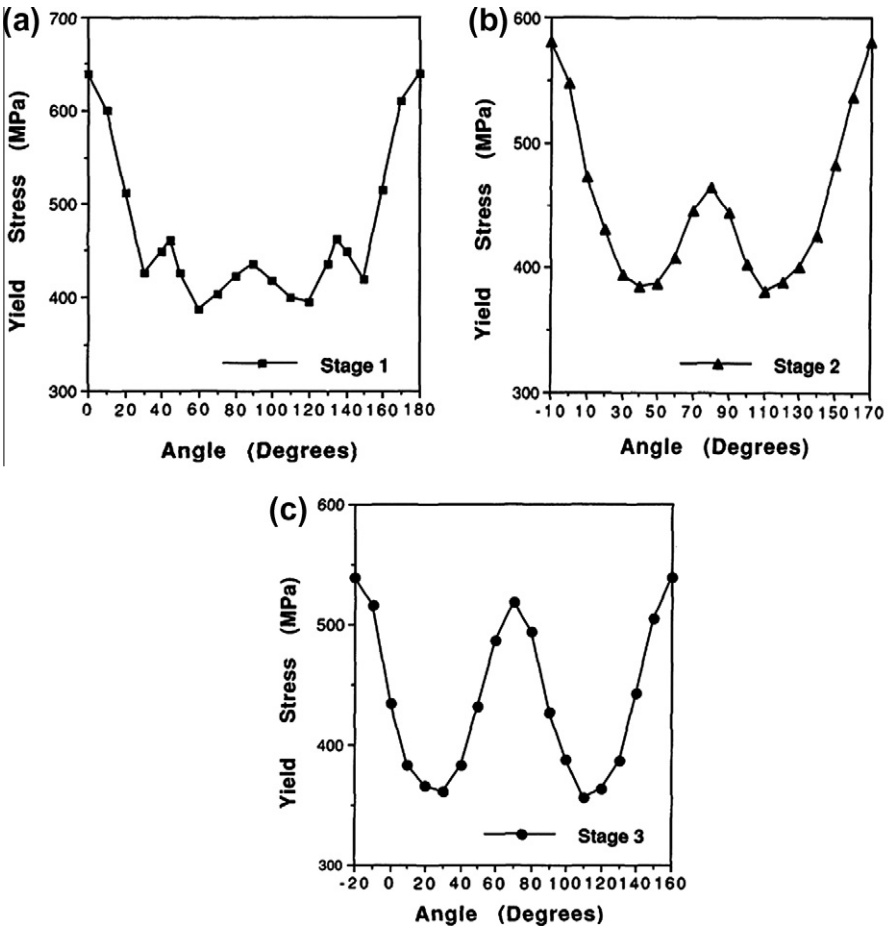

Fig. 1. The σ_u vs. α curves from Mallick et al. (1991): (a) as-received, (b) $\gamma = 0.1$, (c) $\gamma = 0.3$.

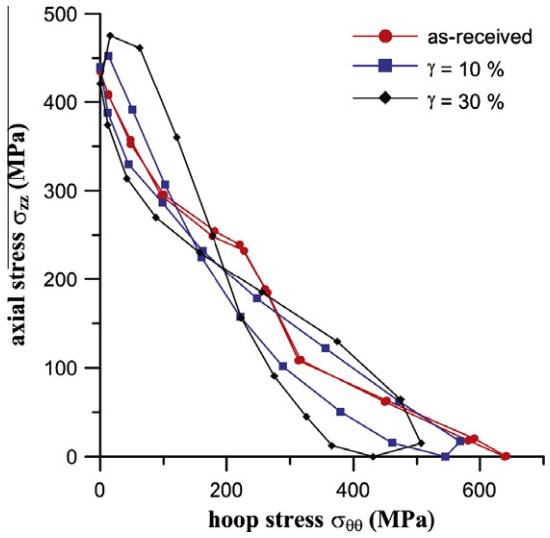

Fig. 2. The plan view of three torsional pre-strains, transformed from experimental data of Fig. 1.

and $\sigma_{\theta z}$ the vertical axis normal to it. The initial yield surface for an isotropic material is an ellipsoid in this space. But, the anisotropic yield surfaces are distorted ellipsoids. The set of points obtained by (1) are points on the surfaces of distorted yield ellipsoids and the positions of these points can be best viewed by the two projections. The first projection is onto the $(\sigma_{\theta\theta} - \sigma_{zz})$ plane (the plan view) and the second projection (the elevation view) is onto a plane that passes through the $\sigma_{\theta z}$ axis and the S_2-direction which is bisecting the right angle formed by the $\sigma_{\theta\theta}$ and $-\sigma_{zz}$ axes. The S_2-direction is the direction of the minor principal axis of the yield ellipsoid of isotropic material. The elevation view would show clearly if there is a rotation of the yield ellipsoid around its major principal axis. After transforming the experimental σ_u vs. α curves in Mallick et al. (1991) into the $(\sigma_{\theta\theta} - \sigma_{zz} - \sigma_{\theta z})$ space by Eq. (1), plan view and elevation view are plotted as shown in Figs. 2 and 3. To our surprise, rotation of the yield surface was observed in the elevation view. Results showed that the yield surfaces of anisotropic material rotated even with a proportional pre-strain path in torsion. The rotation of yield surface had been discussed in some articles but it was only in the $(\sigma_{zz} - \sigma_{\theta z})$ or $(\sigma_{\theta\theta} - \sigma_{zz})$ spaces with

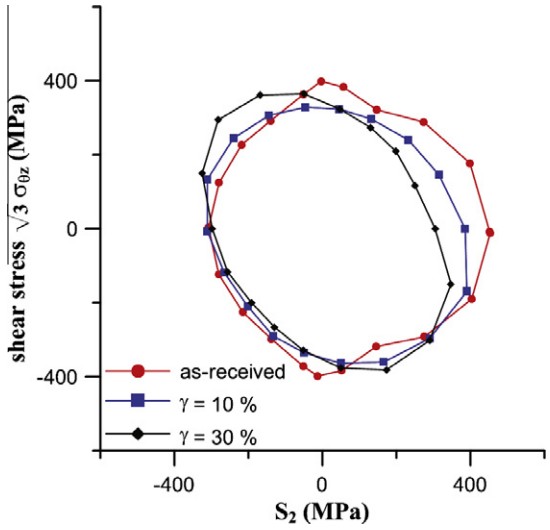

Fig. 3. The elevation view of three torsional pre-strains, transformed from experimental data of Fig. 1.

non-proportional paths (Ishikawa, 1997;Kaneko et al., 1976; Shiratori et al., 1974). Although a slight rotation was found in Fig. 12 of Phillips and Das (1985), the rotation of the yield surface was not discussed in that paper. Because of insufficient experimental results in the $(\sigma_{\theta\theta} - \sigma_{zz} - \sigma_{\theta z})$ space, it gave us the motivation to find out the rotation of subsequent yield surfaces in the $(\sigma_{\theta\theta} - \sigma_{zz} - \sigma_{\theta z})$ space.

3. Specimens and test equipment

The specimens used in experiments were 6061 aluminum alloy tubes, designed for combined loading tests subject to axial, torsion and internal pressure. The gauge section of the specimen was 60 mm long with an outer diameter of 25 mm. The inner diameter was 22 mm and the wall thickness was 1.5 mm with a ratio of radius to thickness of 8.33. Fig. 4 shows the dimensions of the specimen. After machining, the specimens were annealed at a temperature of 410 °C for 2.5 h and the temperature was then lowered slowly to 275 °C in 5 h, and finally they were furnace-cooled to room temperature. In addition, two steel plugs were installed at the ends of tubes and one of them was designed to allow machine oil to run through, in order to apply internal pressure.

The testing machine used for the experiments was a MTS 809 servo hydraulic axial–torsional material testing system. A self-made hydraulic system was used to apply internal pressure, which was an open-loop control system. The load capacity was ±500 kN in tension, ±5500 N-m in torsion and 35 MPa in internal pressure. The axial stress σ_{zz} was obtained by dividing the axial force by the cross-sectional area of the thin-walled specimen. The shear stress $\sigma_{\theta z}$ due to torsion was determined at the mid-thickness of the thin-wall. An MTS 632.80c-04 axial–torsional extensometer with a gauge length of 25 mm was mounted on the specimen to measure axial and shear strains. A PC with LabVIEW 8.6.1 was used to give command voltage to the MTS console and collected signals by NI PCI-6289 DAQ, a data acquisition card which had 4 analog output channels and 32 analog input channels. The card met the demand of controlling 3 channels and acquiring data from 8 sensors simultaneously. The real-time calculation about automated yield point determination was also executed on it.

4. An automated yield stress determination

In earlier experimental determination of yield surface, the process was not fully automated. Investigators had to use their judgments in the determination of yield points. A fully automated method for the yield point determination was introduced and applied to the research work reported in this paper.

Because of special characteristics of servo-controlled hydraulic systems, the loading method could not be the same as that used for dead-load machines. The constant rate loading method was adopted when determining yield points. However, the traditional criterion of yielding, defined by deviation from elastic linearity, needed modification because of data scatter in the servo-controlled system.

The scatter of data was affected by factors related to the equipment such as actuators, the extensometer, the hydraulic system, etc. It was common that the scatter of data varied during an experiment. In the constant rate loading method, if the difference of scatter was too large in one experiment, the results of experiments with traditional yield criterion would be poor. Therefore, for the purpose of automation, scatter of data must be taken into consideration by way of probability when determining yield points.

For each experiment, a pre-test of loading/unloading was conducted within the range of one-third yield stress to eliminate any contact gaps between the specimen and the test equipment. Then,

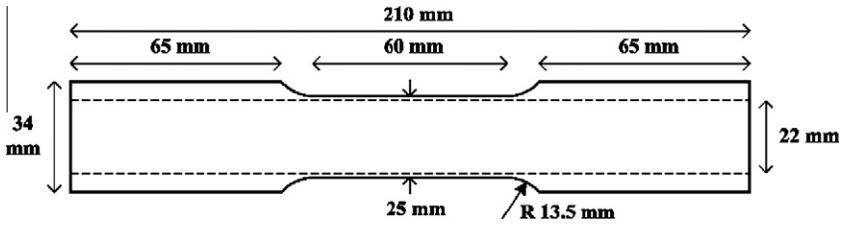

Fig. 4. Test specimens.

in each test, data of the first 4–6 MPa were collected to evaluate model parameters, such as slope and intercept, by linear regression. After calculating the parameters, deviations δ_{dev} of those data from the fitted straight line were calculated from

$$\delta_{dev} = \left[\left(\sigma_{ij}^{(observed)} - \sigma_{ij}^{(fitted)}\right)\left(\sigma_{ij}^{(observed)} - \sigma_{ij}^{(fitted)}\right)\right]^{1/2} \quad (2)$$

Because the controlled paths in the reported experiments were mainly related to the axial and shear strains, and not to the hoop strain, Eq. (2) was expanded as

$$\delta_{dev} = \left\| \begin{bmatrix} \sigma_{zz} \\ \sigma_{\theta z} \end{bmatrix}_{(observed)} - \left(\begin{bmatrix} E & 0 \\ 0 & 2G \end{bmatrix} \begin{bmatrix} \varepsilon_{zz} \\ \varepsilon_{\theta z} \end{bmatrix}_{(observed)} + \begin{bmatrix} b_{zz} \\ b_{\theta z} \end{bmatrix} \right) \right\| \quad (3)$$

where ε_{zz}, $\varepsilon_{\theta z}$ were axial strain and shear strain, respectively; E and G were Young's modulus and shear modulus, respectively; and b_{zz}, $b_{\theta z}$ were the components of "zero offset stress".

The controlled paths were designed to move either along the axial or torsional direction so that only one of E and G in Eq. (3) was used when fitting the experimental curve to the controlled path. The unused E or G would be set to zero to prevent unnecessary noise. The scatter of δ_{dev} calculated from each point of the first 4–6 MPa was studied by Weibull distribution (see Appendix A). Two independent normal distributions with close standard deviations were obtained for axial and torsional directions, respectively. The 95% confidence intervals were used to determine the two parameters of Weibull distribution. Within this model, 99% cumulative probability was taken to evaluate the quantified scatter of data, called δ_{est} (see Fig. 5).

For a specified offset strain ε_{offset}, the yield point was A, with an offset stress of δ_{obj} (see Fig. 5). However, due to data scatter, the point when $\delta_{dev} = \delta_{obj}$ was at B, which had to be corrected by δ_{est} to obtain A. Note that $\delta_{obj}^{(axial)} = E \cdot \varepsilon_{offset}$, $\delta_{obj}^{(torsion)} = G \cdot \gamma_{offset}$ and δ_{est} was the scatter of data as previously explained. Thus, the expression either

$$\delta_{offset}^{(axial)} = \delta_{obj}^{(axial)} - \delta_{est}^{(axial)} \quad (4)$$

or

$$\delta_{offset}^{(torsion)} = \delta_{obj}^{(torsion)} - \delta_{est}^{(torsion)} \quad (5)$$

was used to determine yield point A. In the experiments, $\varepsilon_{offset} = 12.5\ \mu$, $\gamma_{offset} = 25\ \mu$, $E = 72 \sim 65$ GPa and $G = 25 \sim 23$ GPa. E and G varied with pre-strain. If an equivalent offset strain was defined by

$$\bar{\varepsilon} = \left(\varepsilon_{ij}\varepsilon_{ij}\right)^{1/2} = \sqrt{\varepsilon_{11}^2 + 2\varepsilon_{12}^2} \quad (6)$$

then, in the axial probing $\bar{\varepsilon} = \varepsilon_{offset}$, and in torsion probing $\bar{\varepsilon} = \gamma_{offset}/\sqrt{2}$. By use of $\gamma_{offset} = 25\ \mu$, the equivalent strain was found to be $\bar{\varepsilon} = 17.68\ \mu$. Thus, in the experiments $\bar{\varepsilon} \neq \varepsilon_{offset}$ and together with the variation of E led to a variation of, $\delta_{obj}^{(axial)}$ in (4). Similarly, there was a variation of $\delta_{obj}^{(torsion)}$ in (5), because of variation of G. Therefore, Eqs. (4) and (5) become

$$\delta_{offset}^{(axial)} = (0.813 \sim 1.273) - \delta_{est}^{(axial)} \quad (\text{MPa}) \quad (7)$$

$$\delta_{offset}^{(torsion)} = (0.575 \sim 0.625) - \delta_{est}^{(torsion)} \quad (\text{MPa}) \quad (8)$$

In (7), 0.813 was found from $E = 65$ GPa and $\varepsilon_{offset} = 12.5\ \mu$; 1.273 was found from $E = 72$ GPa and $\varepsilon_{offset} = 17.68\ \mu$. These were the extreme cases. In (8), 0.575 was found from $G = 23$ GPa and 0.625 was found from $G = 25$ MPa, both with $\gamma_{offset} = 25\ \mu$. The variation of 0.46 MPa in $\delta_{offset}^{(axial)}$ and 0.05 MPa in $\delta_{offset}^{(torsion)}$ did not lead to noticeable differences in the yield surfaces determined. The yield point was found when $\delta_{dev} = \delta_{offset}$. To make the determination more robust, not only one data point but a certain number of sequential data points were used. The loading rate would also decrease to one-third of original one when $\delta_{dev} \geqslant 0.6\delta_{offset}$. It meant that the loading was slower when approaching the yield point. In this way, the penetration of probing into the plastic region could be minimized.

In all experiments in this research, δ_{est} was between 0.25 MPa and 0.45 MPa and the scatter of internal pressure was within ±0.06 MPa, which could be converted to a ±0.5 MPa hoop stress. In probing yield surfaces, the strain rates were about $\dot{\varepsilon}_{zz} = 2 \times 10^{-6}\ s^{-1}$ and $\dot{\gamma} = 2\dot{\varepsilon}_{z\theta} = 5.5 \times 10^{-6}\ s^{-1}$. Note that it was mentioned by Ellis et al. (1983) and Wu and Yeh (1991) that the probing rate had little effect on the yield surface determination. This automated process of yield stress determination required less manipulation by the operator and it had higher efficiency and decreased artificial errors.

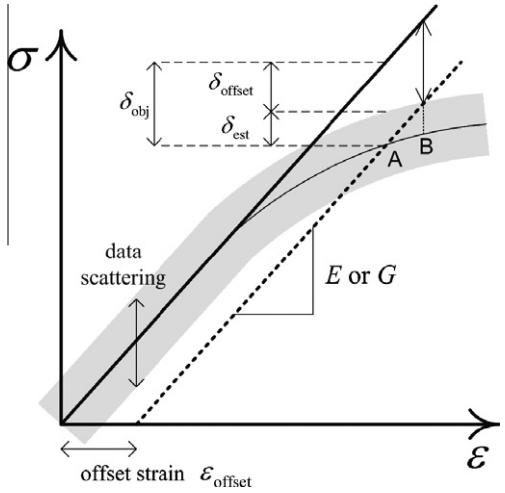

Fig. 5. Automated yield stress determination.

5. Experimental program

This research was concentrated in the investigation of evolution of yield surfaces in the $(\sigma_{zz} - \sigma_{\theta z})$ space and in the $(\sigma_{\theta\theta} - \sigma_{zz} - \sigma_{\theta z})$ space. However, additional experiments were also conducted on the same material to investigate coupled stress–strain behavior in the combined tension–torsion tests of tubular specimens. This

information is useful for further study of plastic deformation and responses.

5.1. Yield surfaces in the $(\sigma_{zz} - \sigma_{\theta z})$ space

Without internal pressure, the initial yield surfaces and the subsequent ones subjected to various axial or torsional pre-strains were probed. The probing path like a fishbone was *O-1-2-3-4-5-6-7-8-9-10-11-12-3-4-O* and changed its direction at *O*, *A*, *B*, *C*, *D* (Fig. 6). The double probing in the pre-strained direction was because of unstable yield stresses on the reverse loading side. Fig. 6 shows the probing paths for specimens with axial pre-strains (path A) and specimens with torsional pre-strains (path B). When probing yield surfaces, the control channels were axial strain and rotation. When applying torsional pre-strains, however, the axial direction was load controlled to keep zero axial stress. This condition is called free-end torsion. Remounting the extensometer was needed because its range of shear strain measurement was $\gamma = 2.18\%$. Because of zero axial stress (free-end), specimens were elongated when applying torsional pre-strains. Therefore, the total shear strain was

$$\gamma_{all} = \gamma_1/(1+\varepsilon_1) + \gamma_2/(1+\varepsilon_2) + \cdots + \gamma_n/(1+\varepsilon_n) \tag{9}$$

where γ_{all} was the shear strain after remounting the extensometer n times. ε_i and γ_i were strain readings from the extensometer at the end of remounting number i. However, the change of the axial strain was much smaller than 1 for this experiment subjected to torsional pre-straining so that γ_{all} could just be the sum of each shear strain. After pre-straining, the stress was reduced to a point close to the center of the subsequent yield surface, and then the specimens were relaxed for one hour before probing the yield surface.

5.2. Yield surfaces in the $(\sigma_{\theta\theta} - \sigma_{zz} - \sigma_{\theta z})$ space

In the $(\sigma_{\theta\theta} - \sigma_{zz} - \sigma_{\theta z})$ space, the load control was applied in the axial direction with increasing or decreasing internal pressure. In that manner, if the internal pressure p was specified, the axial stress and hoop stress of the specimen were

$$\sigma_{zz} = \frac{\pi r^2 p}{\pi(R^2 - r^2)} = \frac{p}{(R/r+1)(R/r-1)} \tag{10}$$

$$\sigma_{\theta\theta} = \frac{2pr}{2(R-r)} = \frac{p}{R/r-1} \tag{11}$$

where R denotes the outer radius and r the inner radius, respectively. The ratio of $\sigma_{\theta\theta}$ to σ_{zz} was $(R/r+1)$, which was close to 2 under thin-walled tube assumption. One special caution was that σ_{zz} should not be read directly from the load cell mounted on the MTS frame when applying internal pressure. Because of load control, the value read out from the load cell was constant during changing internal pressure. However, the axial stress actually had varied due to the change of internal pressure. Therefore, after the internal pressure had stabilized, the reference point (zero point) of the load cell was altered to the value that the specimen was actually subjected to. When pressurizing internally, the loading moved along the path of $\sigma_{\theta\theta} = 2\sigma_{zz}$, shown by dotted line in the $(\sigma_{\theta\theta} - \sigma_{zz} - \sigma_{\theta z})$ space of Fig. 7. The shear stress $\sigma_{\theta z}$ was again determined at the mid-thickness of the thin-wall.

With or without torsional pre-strain and at a specified hoop stress, the probing path in the $(\sigma_{\theta\theta} - \sigma_{zz} - \sigma_{\theta z})$ space was *A-1-2-3-4-3-4-5-6-5-6-7-8-7-8-A*, shown in Fig. 7. In the experiment, the internal pressure was first increased and the stress point moved from center of yield surface *O* to point *A* in Fig. 7. The stress point moved from *A* to *B*, *C* or *D* by applying tensile or compressive axial stress; and it moved along the shear stress direction such as *B3*, *B4*, and *C5* by applying torsion. The probing path lay in a plane parallel to the $(\sigma_{zz} - \sigma_{\theta z})$ plane. The probing paths at different constant hoop stresses lay in different parallel planes. The yield points along the torsional direction were probed twice to obtain more data points. *A*, *B*, *C*, *D* were special points with meanings of $\sigma_{\theta\theta} = 2\sigma_{zz}$, $\sigma_{\theta\theta} = \sigma_{zz}$, $\sigma_{\theta\theta} = -\sigma_{zz}$, $\sigma_{zz} = 0$, respectively. The union of *B* points was a straight line called the S_1 axis, which bisects the right angle formed by the $\sigma_{\theta\theta}$ and σ_{zz} axes. The union of *C* points was another line called the S_2 axis (same as S_2-direction in Section 2), which bisects the right angle formed by the $\sigma_{\theta\theta}$ and $-\sigma_{zz}$ axes. After obtaining yield surfaces in sections with different hoop stresses and parallel to the $(\sigma_{zz} - \sigma_{\theta z})$ space, experimental data could be shown in four special stress spaces, called $(\sigma_{\theta\theta} - \sigma_{zz})$, $(S_1 - \sigma_{\theta z})$, $(\sigma_{\theta\theta} - \sigma_{\theta z})$, $(S_2 - \sigma_{\theta z})$, to demonstrate the ellipsoidal yield surface in the $(\sigma_{\theta\theta} - \sigma_{zz} - \sigma_{\theta z})$ space. By considering the results of this section and Section 5.1 together, ellipsoidal yield surfaces of different torsional and axial pre-strains in the $(\sigma_{\theta\theta} - \sigma_{zz} - \sigma_{\theta z})$ space could be clearly visualized.

The S_1 and S_2-directions are respectively the major and minor principal directions of the yield ellipsoid of the isotropic material. In the present case of anisotropic material, these were not principal directions, but these directions were helpful in the visualization of the evolved 3D yield ellipsoid. The yield curves in the aforementioned $(\sigma_{\theta\theta} - \sigma_{zz})$, $(S_1 - \sigma_{\theta z})$, $(\sigma_{\theta\theta} - \sigma_{\theta z})$, $(S_2 - \sigma_{\theta z})$ stress subspaces were the intersection curves of the yield ellipsoid was cut by the four planes. In addition, the yield curves presented in Section 5.1 were the yield ellipsoid was cut by the $(\sigma_{zz} - \sigma_{\theta z})$ plane.

5.3. Tension–torsion tests

In addition to evolution of the yield surface, tension–torsion tests were conducted by displacement and rotation control in each

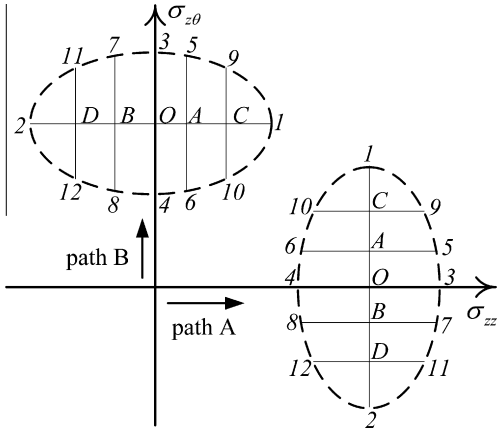

Fig. 6. Probing sequence for two loading paths in the $(\sigma_{zz} - \sigma_{\theta z})$ space.

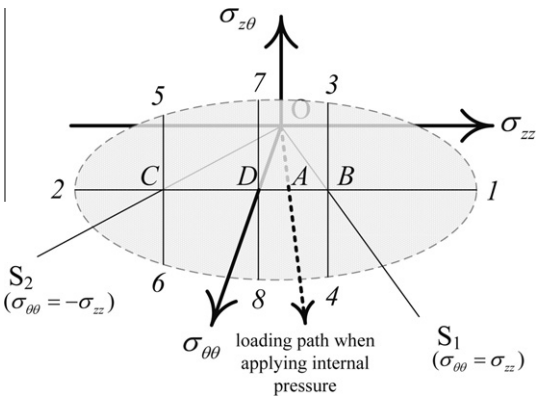

Fig. 7. Probing sequence and the loading path in the $(\sigma_{\theta\theta} - \sigma_{zz} - \sigma_{\theta z})$ space.

control channel to study plastic behavior at large deformation. The specimens were subjected to various tensile strains first. Then, they were subjected to torsion with increasing shear strain while keeping the length of specimen constant (fixed-end torsion). The test continued until buckling occurred. Remounting the extensometer was needed in this experiment because the measuring range of strains for the extensometer were only $\varepsilon = 4.8\%$ and $\gamma = 2.18\%$. During axial pre-straining, the measured axial strain should be modified due to remounting, as:

$$\varepsilon_{\text{all}} = (1+\varepsilon_1)(1+\varepsilon_2)\cdots(1+\varepsilon_n) - 1 \tag{12}$$

where ε_{all} was the axial strain after remounting and ε_i were axial strain readings from the extensometer at the end of remounting number i. During fixed-end torsion, the measured shear strain was the sum of all shear strain readings of all re-mountings. Eq. (9) did not apply in this case.

The results of these tests can be used to verify constitutive models. Although similar tests have been conducted by other investigators, the present tests were conducted on the same material as that used in the determination of the yield surfaces in Sections 5.1 and 5.2. Therefore, material parameters of the constitutive models can be determined.

6. Results and discussions

6.1. The $(\sigma_{zz} - \sigma_{\theta z})$ space

The initial yield surfaces were probed on most specimens before pre-straining. Results of 10 specimens are shown in Fig. 8. The dotted circle represents the von Mises yield surface where the axial and shear yield stresses are ±34 MPa and ±19.6 MPa, respectively.

Only one specimen was used to obtain subsequent yield surfaces with axial pre-strains of 0.5%, 1.0%, 3.0% and 4.0%. Experimental results of axial pre-strains 0.5% and 1.0% are shown in Fig. 9 together with the initial yield surface. Results of axial pre-strains 3.0% and 4.0% are shown in Fig. 10. All yield surfaces of different pre-strains are summarized in Fig. 11. The yield surfaces of axial pre-strain 0.5% are similar to flattened ellipses with flattened rear parts and rounded nose. This characteristic is not clearly shown for the cases with the axial pre-strains of 3% and 4%. The rear sides of axial pre-strains 3% and 4% almost coincide. However, it is interesting that the size of yield surfaces decreased first and then increased after an axial pre-strain of 1.0%.

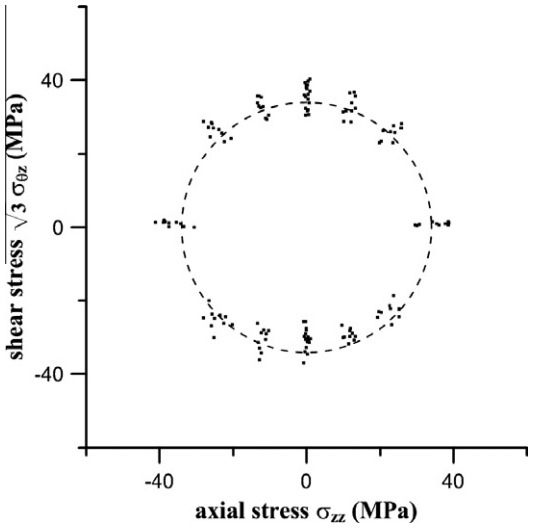

Fig. 8. The initial yield surface.

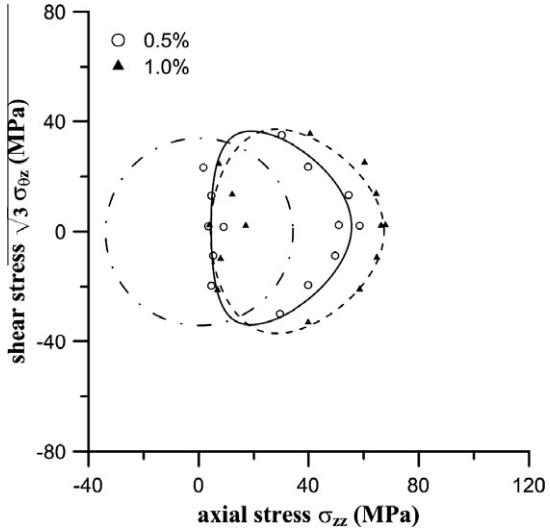

Fig. 9. The subsequent yield surfaces of axial pre-strains 0.5% and 1.0% compared with the initial yield surface.

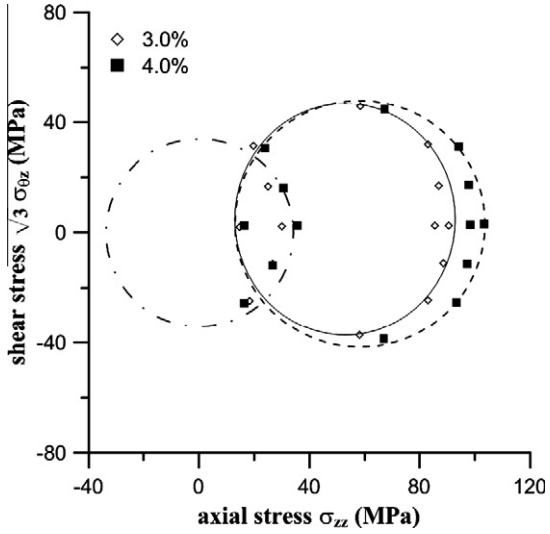

Fig. 10. The subsequent yield surfaces of axial pre-strains 3.0% and 4.0% compared with the initial yield surface.

After probing the subsequent yield surface with an axial pre-strain of 4%, the specimen was unloaded to zero axial stress. Then, it was loaded again to reach the same axial stress as previously obtained with an axial pre-strain of 4%. The subsequent yield surface was probed again and the result is shown together with the previous one in Fig. 12. The yield surface determined after reloading was a little larger but it could be regarded as a good approximation of the original yield surface with an axial pre-strain of 4%. This experimental evidence showed that, despite possible inaccuracy mentioned by Khan et al. (2009), the yield surface probed after unloading followed by reloading to its original stress would provide a good approximated yield surface (Wu, 2003).

Six specimens were used to determine subsequent yield surfaces with torsional pre-strains of 0.144%, 0.5%, 1.0%, 3.0% and 6.0%. Experimental results of axial pre-strains 0.144% and 0.5% are shown in Fig. 13. In each case of 1.0%, 3.0% and 6.0% pre-strains, experiments were conducted on two specimens. Results of torsional pre-strains 1.0%, 3.0% and 6.0% are shown in Figs. 14–16, respectively. All yield surfaces with different pre-strains are summarized in Fig. 17. The behavior of this set of yield surfaces was

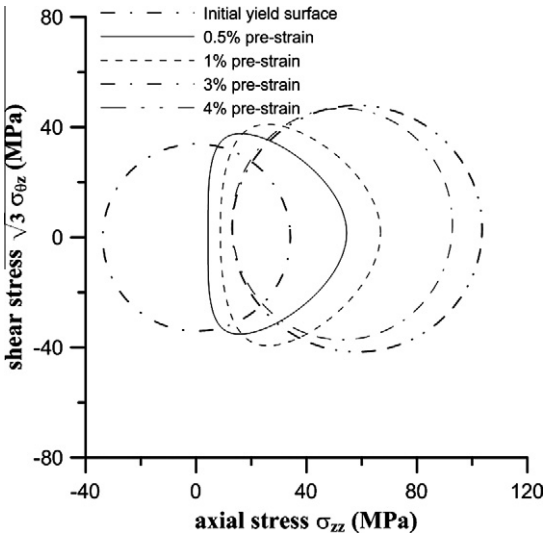

Fig. 11. A summary of yield surfaces from Figs. 8 and 9.

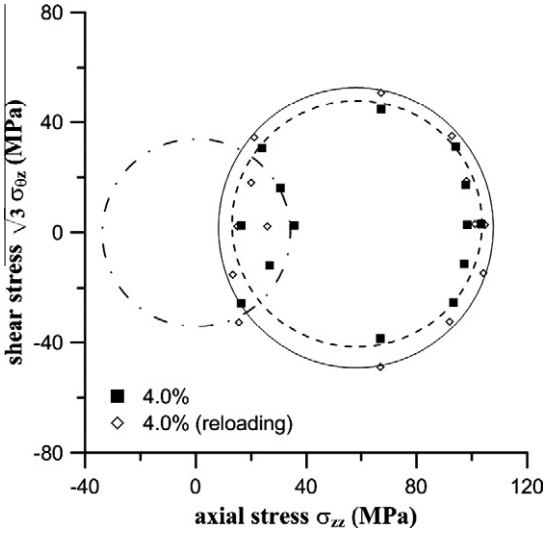

Fig. 12. Comparison of yield surface probed after reloading to that probed at initial loading.

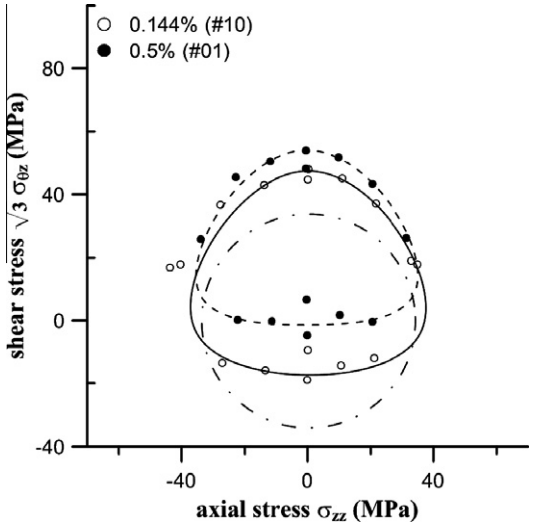

Fig. 13. The subsequent yield surfaces of torsional pre-strains 0.144% and 0.5% compared with the initial yield surface.

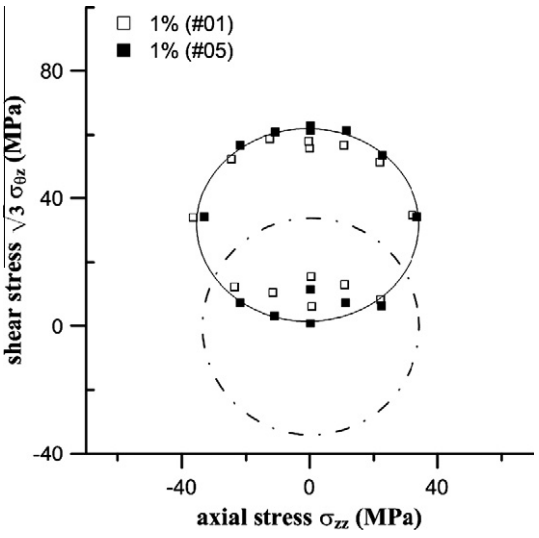

Fig. 14. The subsequent yield surface of torsional pre-strain 1.0% compared with the initial yield surface.

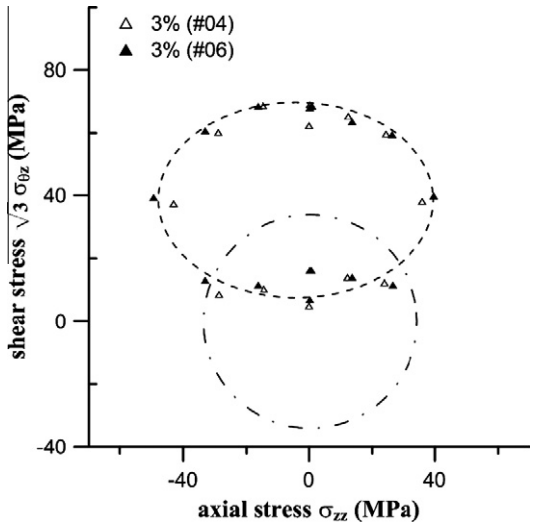

Fig. 15. The subsequent yield surface of torsional pre-strain 3.0% compared with the initial yield surface.

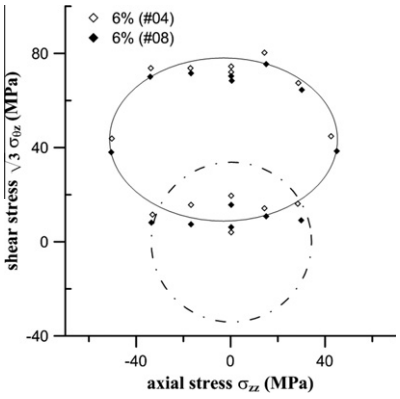

Fig. 16. The subsequent yield surface of torsional pre-strain 6.0% compared with the initial yield surface.

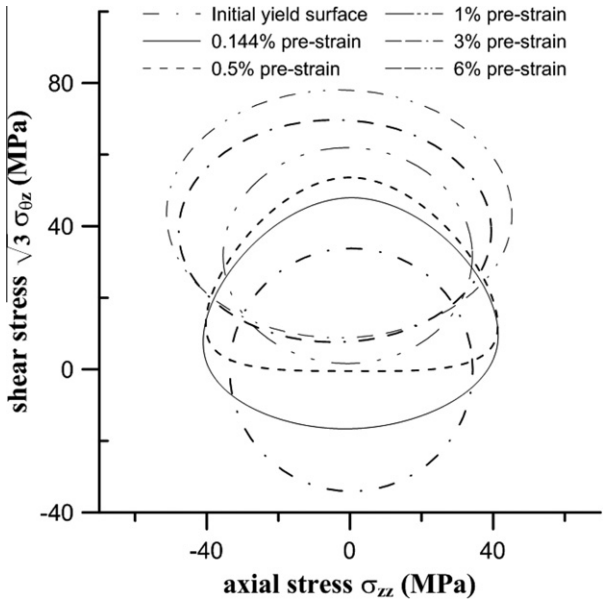

Fig. 17. A summary of yield surfaces from Figs. 12–15.

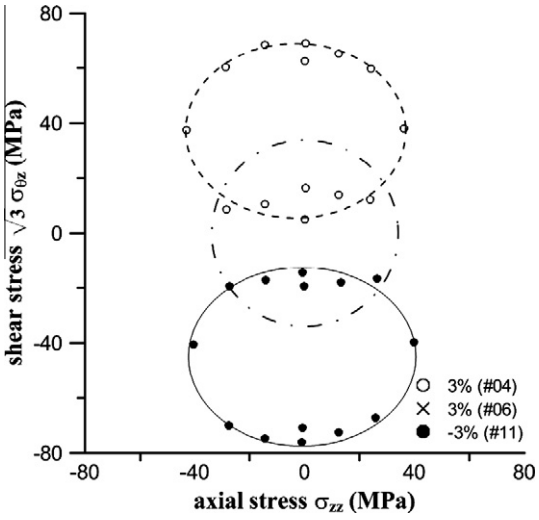

Fig. 18. The subsequent yield surfaces of torsional pre-strain −3.0% and 3.0% compared with the initial yield surface.

similar to those with axial pre-strains. The shapes of yield surfaces gradually became ellipses and 1.0% torsional pre-strain was also a dividing point about the size of the yield surface and cross effect. The size of the yield surface decreased first at small pre-strain and increased when the pre-strain was larger than 1.0%. The subsequent yield surface of a reversed torsional pre-strain −3% was also probed and the results compared with the one with a pre-strain of 3% in Fig. 18. It is seen that the results of the two cases are symmetric with respect to the σ_{zz} axis.

6.2. The $(\sigma_{\theta\theta} - \sigma_{zz} - \sigma_{\theta z})$ space

The initial yield surfaces probed on two specimens in the $(\sigma_{\theta\theta} - \sigma_{zz} - \sigma_{\theta z})$ space are presented in the $(\sigma_{\theta\theta} - \sigma_{zz})$, $(S_1 - \sigma_{\theta z})$, $(\sigma_{\theta\theta} - \sigma_{\theta z})$ and $(S_2 - \sigma_{\theta z})$ spaces, and shown in Figs. 19–22, respectively. Results of the two specimens were quite compatible. Initial anisotropy was observed in the $(\sigma_{\theta\theta} - \sigma_{zz})$ space in which the hoop

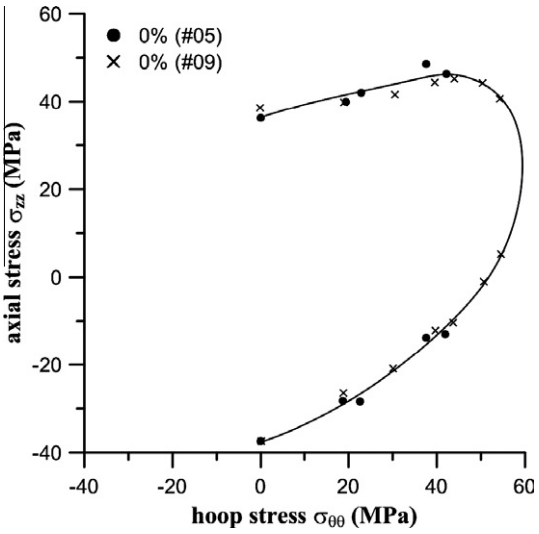

Fig. 19. The initial yield surface in the $(\sigma_{\theta\theta} - \sigma_{zz})$ space.

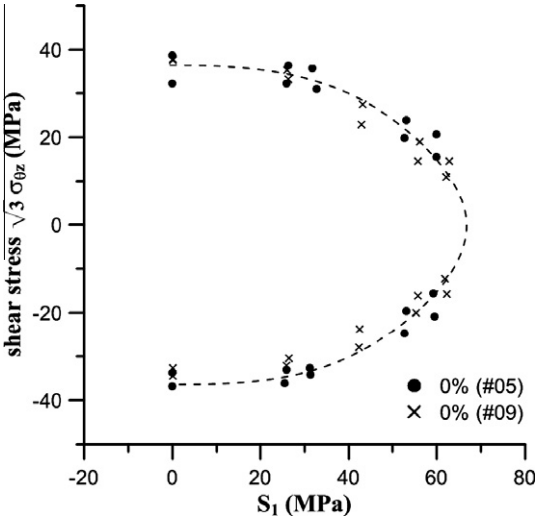

Fig. 20. The initial yield surface in the $(S_1 - \sigma_{\theta z})$ space.

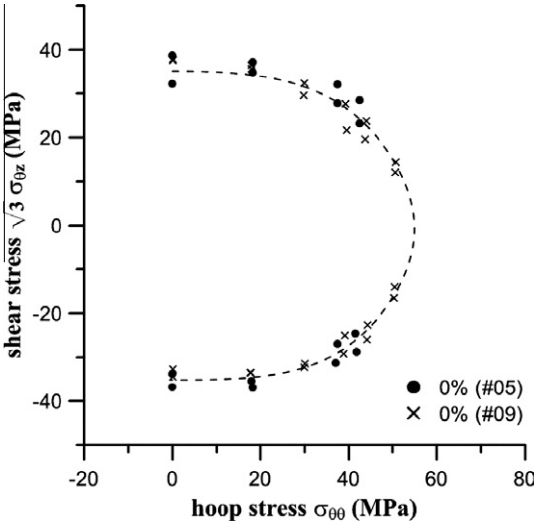

Fig. 21. The initial yield surface in the $(\sigma_{\theta\theta} - \sigma_{\theta z})$ space.

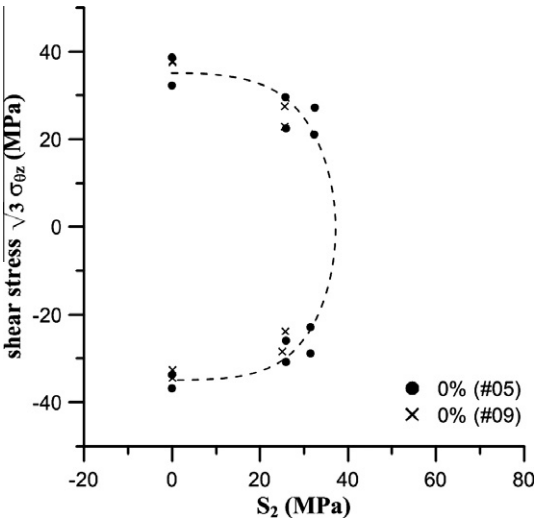

Fig. 22. The initial yield surface in the $(S_2 - \sigma_{\theta z})$ space.

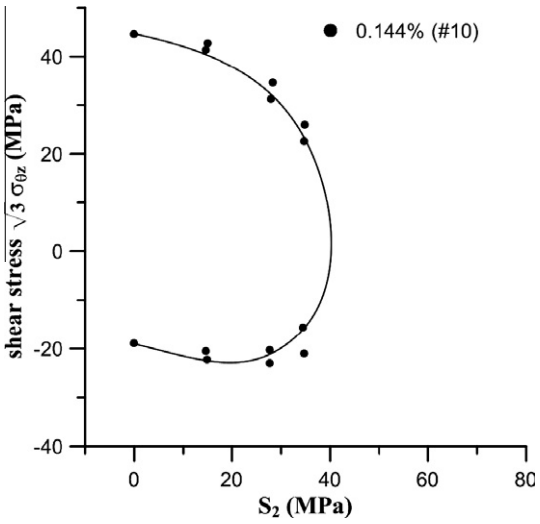

Fig. 25. The subsequent yield surface of torsional pre-strain 0.144% in the $(S_2 - \sigma_{\theta z})$ space.

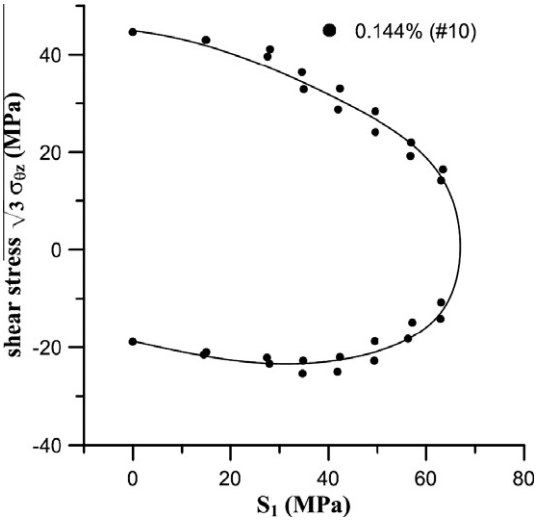

Fig. 23. The subsequent yield surface of torsional pre-strain 0.144% in the $(S_1 - \sigma_{\theta z})$ space.

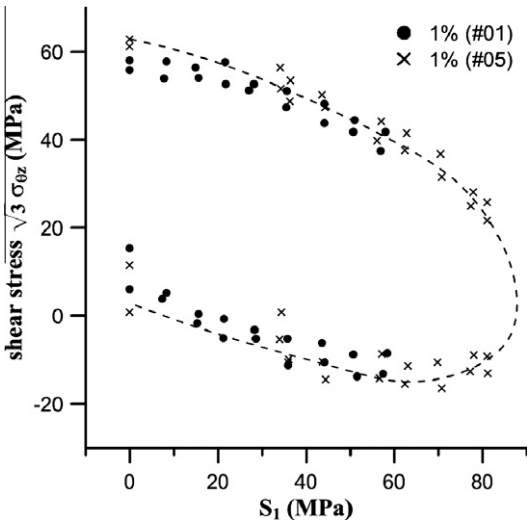

Fig. 26. The subsequent yield surface of torsional pre-strain 1.0% in the $(S_1 - \sigma_{\theta z})$ space.

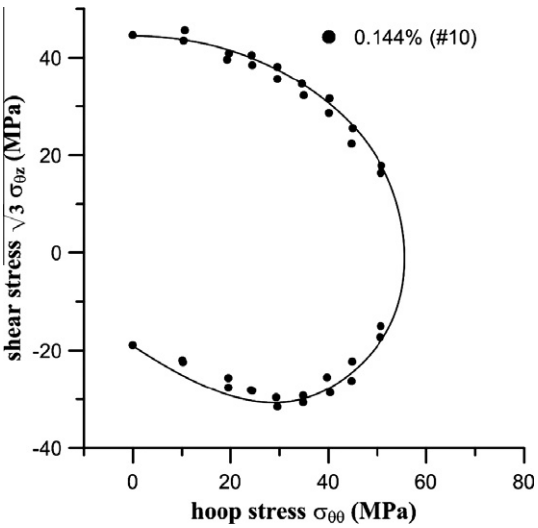

Fig. 24. The subsequent yield surface of torsional pre-strain 0.144% in the $(\sigma_{\theta\theta} - \sigma_{\theta z})$ space.

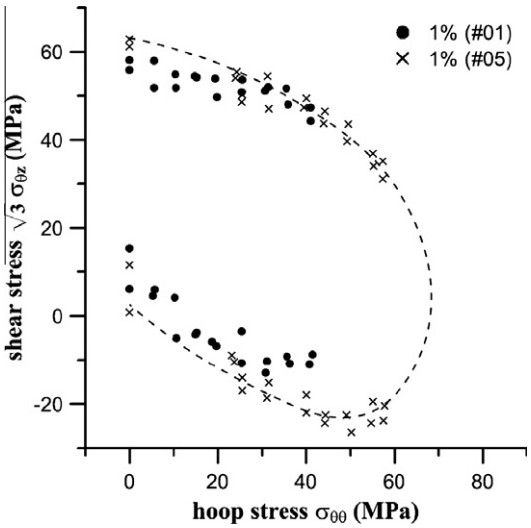

Fig. 27. The subsequent yield surface of torsional pre-strain 1.0% in the $(\sigma_{\theta\theta} - \sigma_{\theta z})$ space.

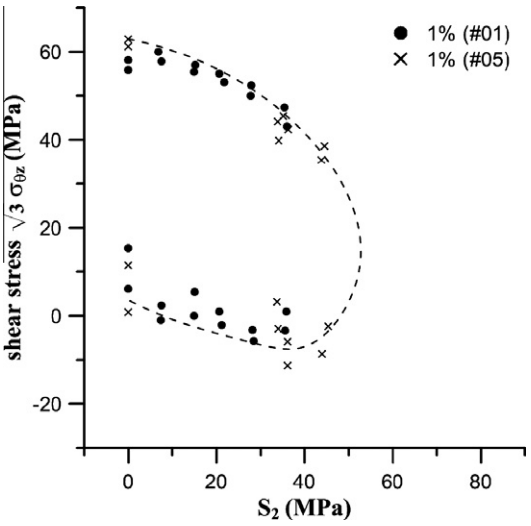

Fig. 28. The subsequent yield surface of torsional pre-strain 1.0% in the $(S_2 - \sigma_{\theta z})$ space.

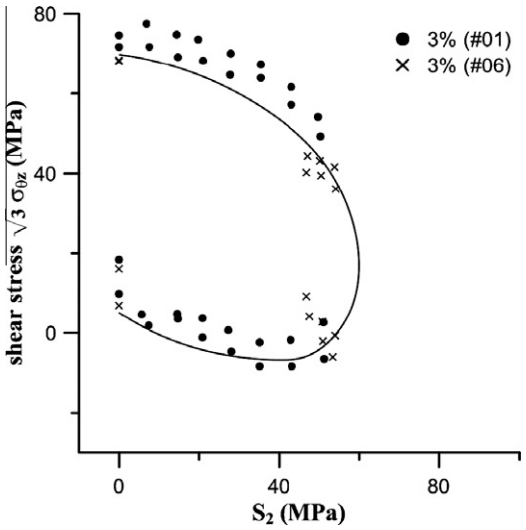

Fig. 31. The subsequent yield surface of torsional pre-strain 3.0% in the $(S_2 - \sigma_{\theta z})$ space.

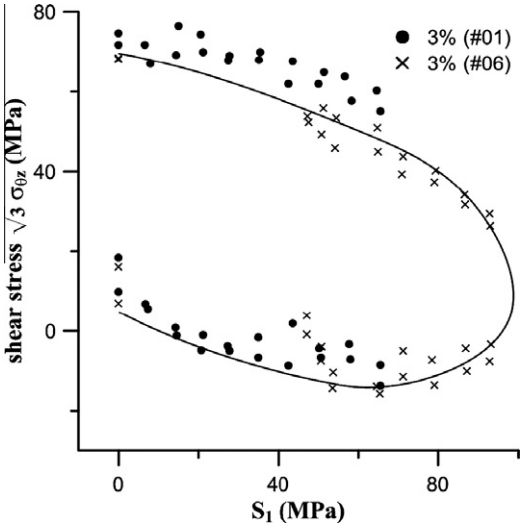

Fig. 29. The subsequent yield surface of torsional pre-strain 3.0% in the $(S_1 - \sigma_{\theta z})$ space.

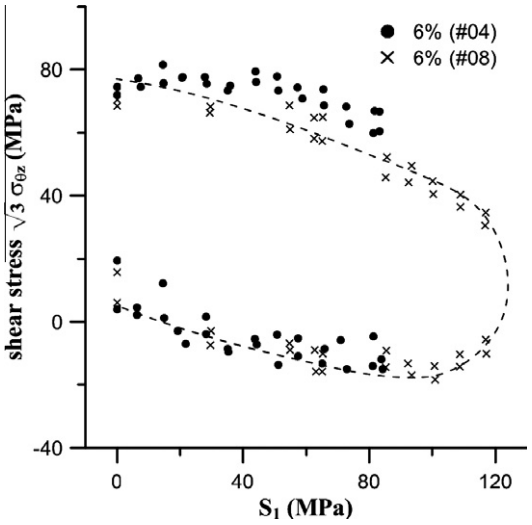

Fig. 32. The subsequent yield surface of torsional pre-strain 6.0% in the $(S_1 - \sigma_{\theta z})$ space.

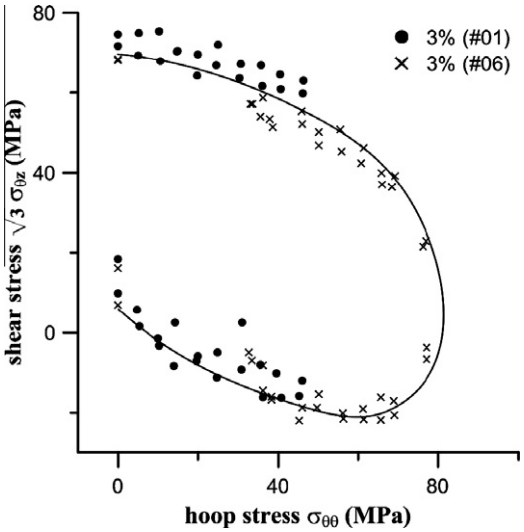

Fig. 30. The subsequent yield surface of torsional pre-strain 3.0% in the $(\sigma_{\theta\theta} - \sigma_{\theta z})$ space.

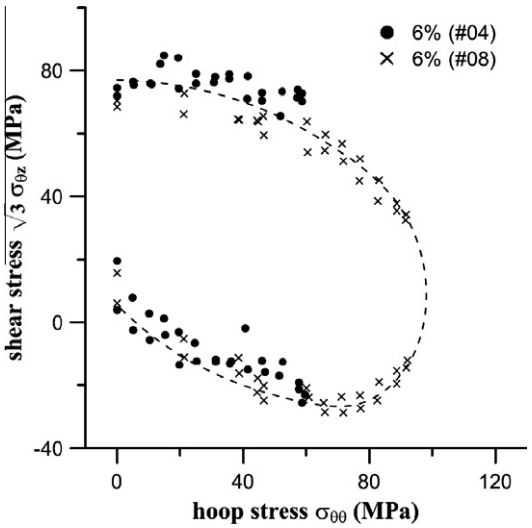

Fig. 33. The subsequent yield surface of torsional pre-strain 6.0% in the $(\sigma_{\theta\theta} - \sigma_{\theta z})$ space.

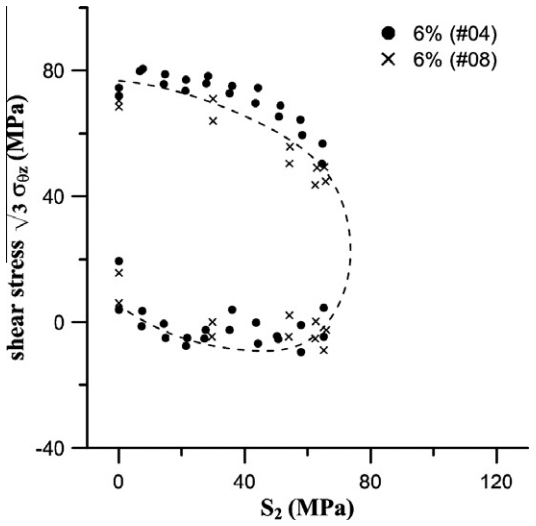

Fig. 34. The subsequent yield surface of torsional pre-strain 6.0% in the $(S_2 - \sigma_{\theta z})$ space.

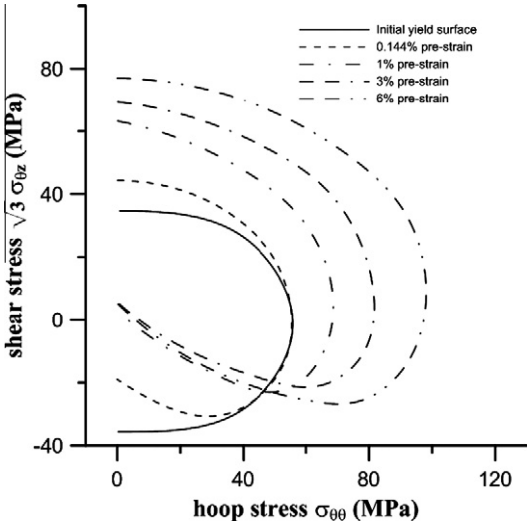

Fig. 36. A summary of yield surfaces in the $(\sigma_{\theta\theta} - \sigma_{\theta z})$ space from Figs. 20, 23, 26, 29 and 32.

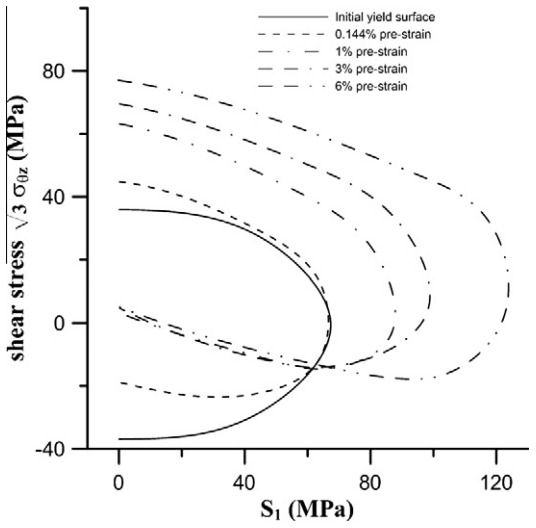

Fig. 35. A summary of yield surfaces in the $(S_1 - \sigma_{\theta z})$ space from Figs. 19, 22, 25, 28 and 31.

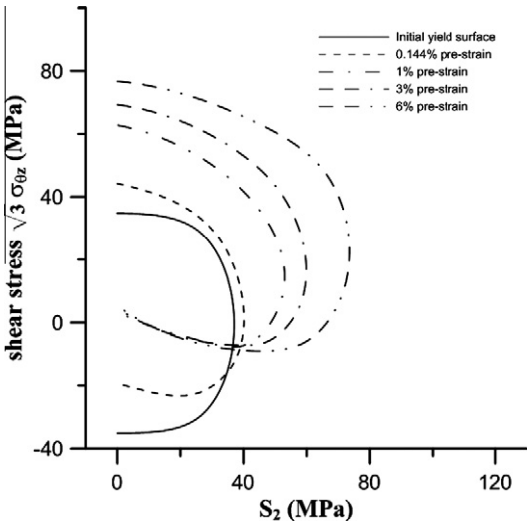

Fig. 37. A summary of yield surfaces in the $(S_2 - \sigma_{\theta z})$ space from Figs. 21, 24, 27, 30 and 33.

yield stress was larger than the axial yield stress. The von Mises yield criterion which described the initial yield surface well in the $(\sigma_{zz} - \sigma_{\theta z})$ space was not able to describe the initial yield surface in the $(\sigma_{\theta\theta} - \sigma_{zz} - \sigma_{\theta z})$ space.

With different torsional pre-strains of 0.144%, 1.0%, 3.0% and 6.0%, yield surfaces in the $(S_1 - \sigma_{\theta z})$, $(\sigma_{\theta\theta} - \sigma_{\theta z})$ and $(S_2 - \sigma_{\theta z})$ spaces were experimentally obtained. In these cases, except for 0.144% which had only one specimen, two specimens were used to determine the experimental results of each case. All data points are shown in figures, Figs. 23–25 for 0.144% pre-strain; Figs. 26–28 for 1.0% pre-strain; Figs. 29–31 for 3.0% pre-strain and Figs. 32–34 for 6.0% pre-strain. The results in the $(S_1 - \sigma_{\theta z})$, $(\sigma_{\theta\theta} - \sigma_{\theta z})$ and $(S_2 - \sigma_{\theta z})$ spaces are summarized in Figs. 35–37, respectively. The clockwise rotation of yield surfaces was observed clearly in these figures. The amounts of yield surface rotations were almost the same in the $(S_1 - \sigma_{\theta z})$, $(\sigma_{\theta\theta} - \sigma_{\theta z})$ and $(S_2 - \sigma_{\theta z})$ spaces although the rotation was slightly larger in the $(\sigma_{\theta\theta} - \sigma_{\theta z})$ space. Therefore, it is fair to say that the yield surface rotated around the σ_{zz} axis. The positive cross effect is more obvious than that in the $(\sigma_{zz} - \sigma_{\theta z})$ space when torsional pre-strain was 1.0%.

The test of torsional pre-strain −3% was also conducted to observe the behavior of yield surface in the $(\sigma_{\theta\theta} - \sigma_{zz} - \sigma_{\theta z})$ space under a reverse torsion. Yield surfaces with torsional pre-strains of −3% and 3% are shown together in Figs. 38–40. It is seen that the rotation for specimen with 3% pre-strain was clockwise and that for a specimen with −3% pre-strain was counterclockwise.

Yield surfaces of axial pre-strains in the $(\sigma_{\theta\theta} - \sigma_{zz} - \sigma_{\theta z})$ space were obtained in one specimen. The specimen was subjected to 4% axial pre-strain first and then unloaded to a zero axial stress. After finding out the approximated center of the subsequent yield surface, which was the axial stress of 12.5 MPa in this test, the center was set as the starting point of S_1 and S_2 axes. The yield surfaces probed in the $(S_1 - \sigma_{\theta z})$ and $(S_2 - \sigma_{\theta z})$ spaces did not rotate, and are shown together with the initial yield surfaces in Figs. 41 and 42, respectively. These experimental results showed that the rotation of subsequent yield surfaces was pre-strain path dependent.

6.3. Tension–torsion tests

In the case of free-end torsion, one specimen without axial pre-strain was subjected to a shear strain of 6%. Results in the $(\gamma - \sigma_{\theta z})$

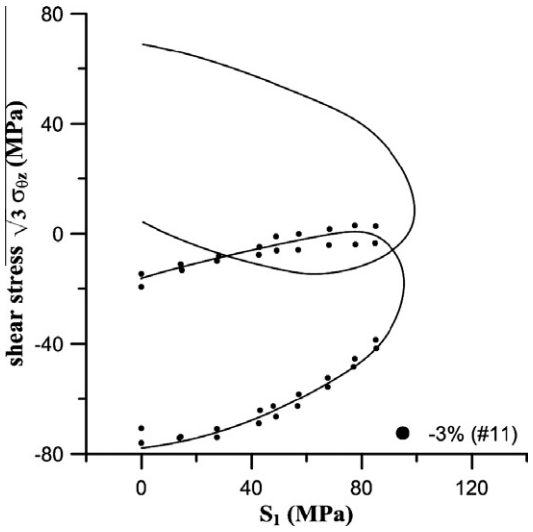

Fig. 38. The subsequent yield surfaces of torsional pre-strain −3.0% and 3.0% in the $(S_1 - \sigma_{\theta z})$ space.

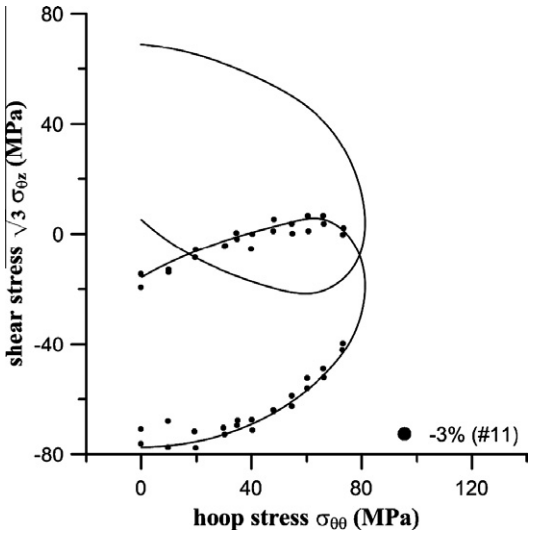

Fig. 39. The subsequent yield surfaces of torsional pre-strain −3.0% and 3.0% in the $(\sigma_{\theta\theta} - \sigma_{\theta z})$ space.

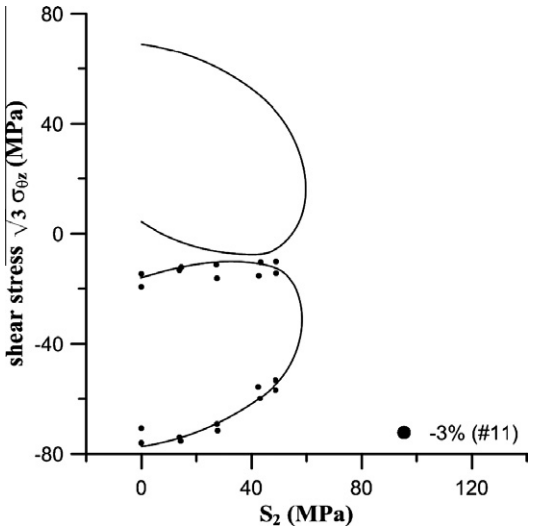

Fig. 40. The subsequent yield surfaces of torsional pre-strain −3.0% and 3.0% in the $(S_2 - \sigma_{\theta z})$ space.

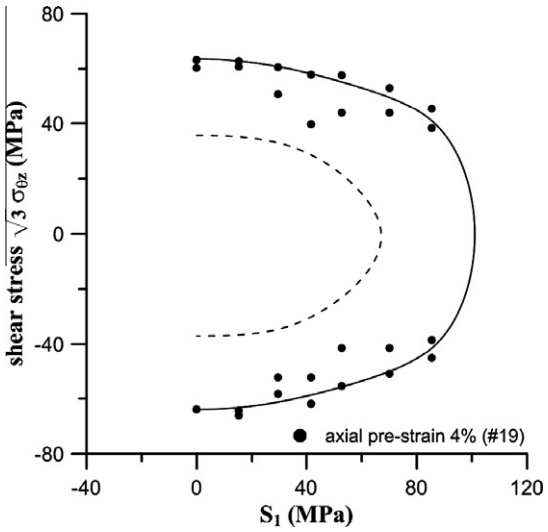

Fig. 41. The subsequent yield surface of axial pre-strain 4.0% in the $(S_1 - \sigma_{\theta z})$ space.

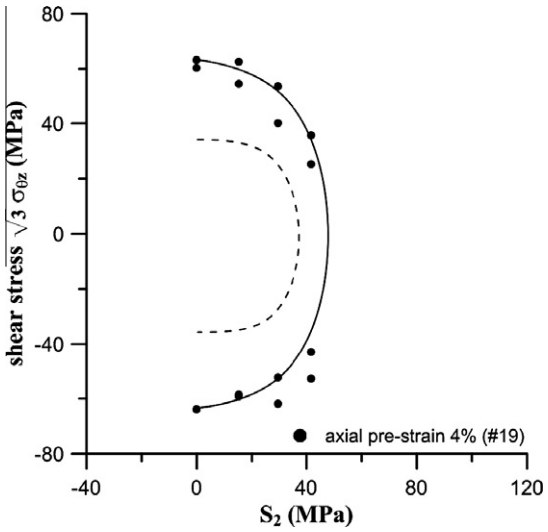

Fig. 42. The subsequent yield surface of axial pre-strain 4.0% in the $(S_2 - \sigma_{\theta z})$ space.

and $(\gamma - \varepsilon_{zz})$ spaces are shown in Figs. 43 and 44. It is seen that the specimen was elongated in the case of free-end torsion.

In the case of fixed-end torsion, five specimens were subjected to different axial pre-strains. Three of these specimens were from a different batch of specimens (Batch B of the same material), not from the same batch used to probe yield surfaces (Batch A). Specimens of Batch B were annealed at 415 °C in 3 h and then furnace-cooled to room temperature. With axial pre-strains of 0.74% (Batch A), 2.5% (Batch B), 4.0% (Batch B), 10% (Batch A) and 10% (Batch B) at $\dot{\varepsilon}_{zz} = 3 \sim 8 \times 10^{-5}\ s^{-1}$, the curves in the $(\varepsilon_{zz} - \sigma_{zz})$ space are shown in Fig. 45. The curve of 10% (Batch B) was a little different from others but results of the two batches were compatible. With each different axial pre-strain, specimens were subjected to a shear strain of up to 13% at $\dot{\gamma} = 1 \sim 2 \times 10^{-5}\ s^{-1}$. Results in the $(\gamma - \sigma_{\theta z})$ and $(\gamma - \sigma_{zz})$ spaces are shown in Figs. 46–48. The effect of axial pre-strains was obvious in the subsequent torsion. In the $(\gamma - \sigma_{\theta z})$ space, curves of smaller axial pre-strains are lower. In the $(\gamma - \sigma_{\theta z})$ space, axial stresses decreased rapidly after torsion started and they approached stable values with increasing shear strains. If buckling did not happen, axial stresses would go into small compression at large shear strains, as in the cases of 0.74% (Batch A)

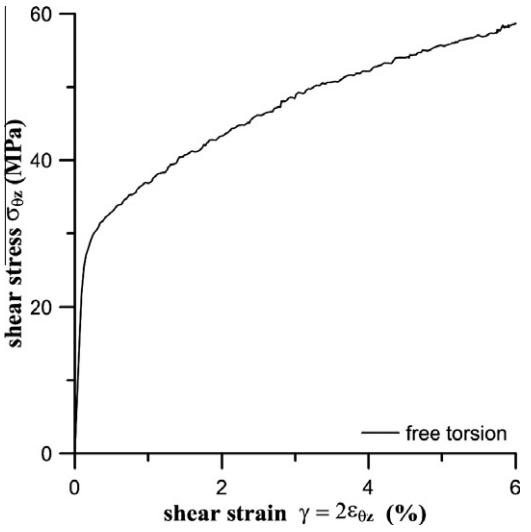

Fig. 43. The shear stress–strain curve of free-end torsion without axial pre-strain.

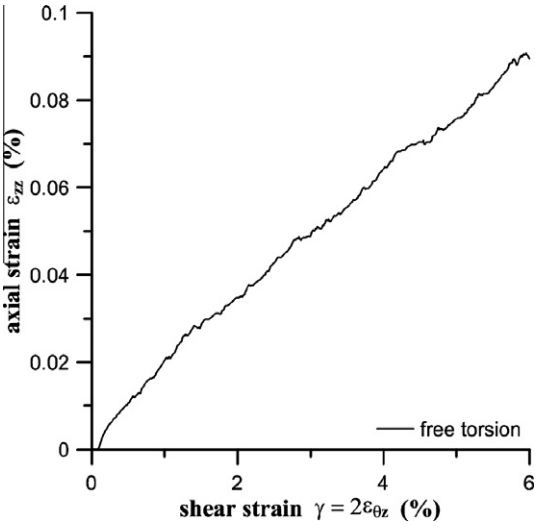

Fig. 44. The ε_{zz} vs. γ curve of free-end torsion without axial pre-strain.

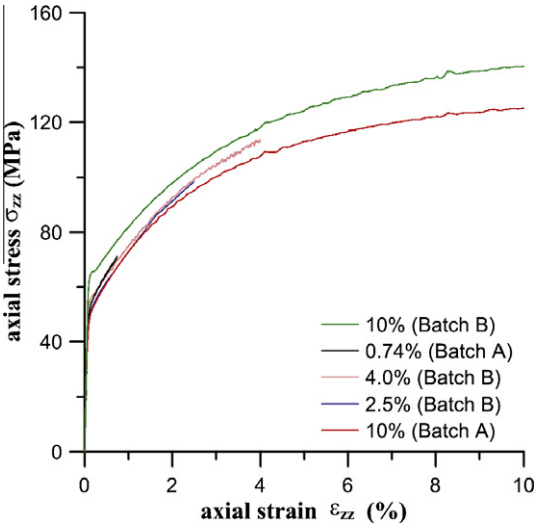

Fig. 45. Axial stress–strain curves of various specimens.

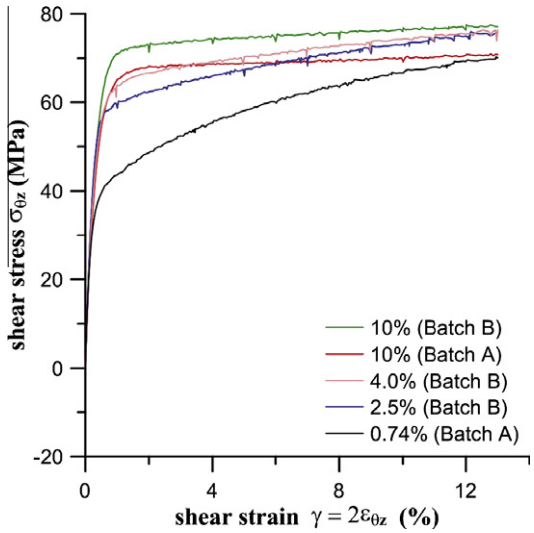

Fig. 46. Shear stress–strain curves for fixed-end torsion.

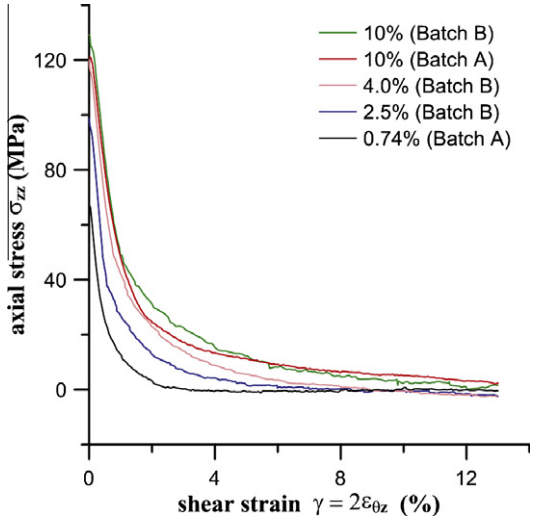

Fig. 47. Axial stress distribution for fixed-end torsion.

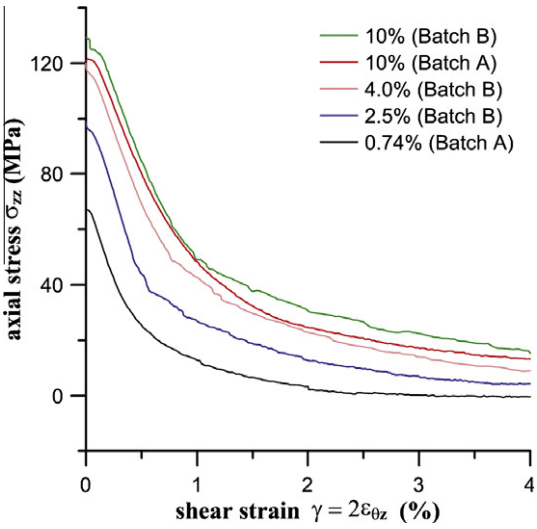

Fig. 48. Axial stress distribution at small shear strain for fixed-end torsion.

and 2.5% (Batch B). Buckling occurred at large shear strains as in the cases of 4.0% (Batch B) and 10% (Batch A, B) pre-strains. The differences between the two batches of specimens can be observed clearly from the curves of 10% pre-strain in Figs. 47 and 48.

7. Conclusions

Three series of experiments were conducted using annealed 6061 aluminum alloy tubes with a servo hydraulic testing system. They were (1) evolution of yield surfaces in the $(\sigma_{zz} - \sigma_{\theta z})$ space; (2) evolution of yield surfaces in the $(\sigma_{\theta\theta} - \sigma_{zz} - \sigma_{\theta z})$ space; (3) combined tension–torsion tests. An automated yield stress determination was used when probing yield surfaces to increase efficiency and decrease artificial errors. The following phenomena have been observed from experimental results.

1. Yield surfaces of various axial or torsional pre-strains in the $(\sigma_{zz} - \sigma_{\theta z})$ space showed noses and unapparent cross effect at small pre-strains. They became ellipses and had positive cross effect with increasing pre-strains. In addition, the size of yield surfaces decreased first and then increased after an axial pre-strain of 1.0%.
2. Initial anisotropy was observed from the initial yield surface in the $(\sigma_{\theta\theta} - \sigma_{zz} - \sigma_{\theta z})$ space. The von Mises yield criterion that seems suitable in the $(\sigma_{zz} - \sigma_{\theta z})$ space is actually inadequate for the $(\sigma_{\theta\theta} - \sigma_{zz} - \sigma_{\theta z})$ space.
3. The rotation of the yield surface was pre-strain path dependent. The clockwise rotation of subsequent yield surfaces shown in the $(S_1 - \sigma_{\theta z})$, $(\sigma_{\theta\theta} - \sigma_{\theta z})$ and $(S_2 - \sigma_{\theta z})$ spaces was observed with various torsional pre-strains. If subjected to a reverse torsion, yield surfaces in these stress spaces would rotate in a reverse direction. On the other hand, experiments showed that, if subjected to axial pre-strains, yield surfaces did not rotate around the σ_{zz} axis. Therefore, the rotation behavior of yield surface is pre-strain path dependent and a theory of plasticity should include a way to account for rotation of the yield surface.
4. A free-end torsion of a thin-walled cylindrical specimen gave rise to specimen elongation. In the combined tension–torsion, with fixed-end condition, the shear stress increased while the axial stress decreased rapidly at small strain levels with increasing shear strain.

Acknowledgement

This research is supported by National Research Council of Taiwan (NSC 97-2221-E-002-120-MY2, 98-2811-E-002-118 and 98-2811-E-002-090).

Appendix A

Taking one set of data during axial loading as an example, the scatters of signals are shown as normal distributions in either axial or shear stress, see Figs. A.1 and A.2. Their probability density functions are

$$f_{\text{axial}} = \frac{1}{\sqrt{2\pi d_{\text{axial}}^2}} \exp\left(\frac{-\left(\sigma_{zz}^{(\text{observed})} - \sigma_{zz}^{(\text{fitted})}\right)^2}{2d_{\text{axial}}^2}\right) \tag{A.1}$$

$$f_{\text{torsion}} = \frac{1}{\sqrt{2\pi d_{\text{torsion}}^2}} \exp\left(\frac{-\left(\sigma_{\theta z}^{(\text{observed})} - \sigma_{\theta z}^{(\text{fitted})}\right)^2}{2d_{\text{torsion}}^2}\right) \tag{A.2}$$

where d is standard deviation. The subscripts "axial" and "torsion" denote, respectively, the axial direction and torsion direction. If two

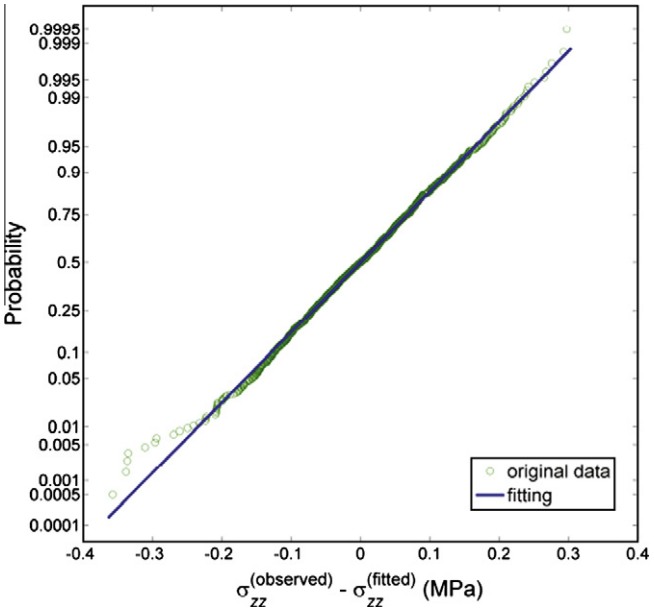

Fig. A.1. The probability plot of $\left(\sigma_{zz}^{(\text{observed})} - \sigma_{zz}^{(\text{fitted})}\right)$ and fitted normal distribution.

normal distributions are independent and $d_{\text{axial}} = d_{\text{torsion}}$, the probability density function of occurrence of δ_{dev} is

$$g = 2\pi\delta_{\text{dev}} f_{\text{axial}} f_{\text{torsion}} = \frac{\delta_{\text{dev}}}{d^2} \exp\left(\frac{-\delta_{\text{dev}}^2}{2d^2}\right) \tag{A.3}$$

where $\delta_{\text{dev}} = \left[\left(\sigma_{zz}^{(\text{observed})} - \sigma_{zz}^{(\text{fitted})}\right)^2 + \left(\sigma_{\theta z}^{(\text{observed})} - \sigma_{\theta z}^{(\text{fitted})}\right)^2\right]^{1/2}$ and $d = d_{\text{axial}} = d_{\text{torsion}}$. By setting $k = 2$, $x = \delta_{\text{dev}}$, and $\lambda = \sqrt{2}d$, the probability density function of Weibull distribution

$$W = \frac{k}{\lambda}\left(\frac{x}{\lambda}\right)^{k-1} \exp\left(\frac{-x^k}{\lambda^k}\right), \quad x \geqslant 0 \tag{A.4}$$

becomes Eq. (A.3).

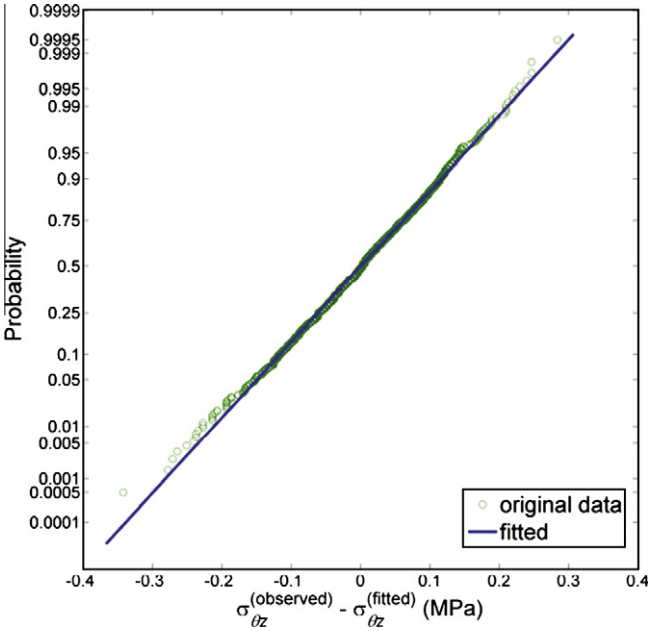

Fig. A.2. The probability plot of $\left(\sigma_{\theta z}^{(\text{observed})} - \sigma_{\theta z}^{(\text{fitted})}\right)$ and fitted normal distribution.

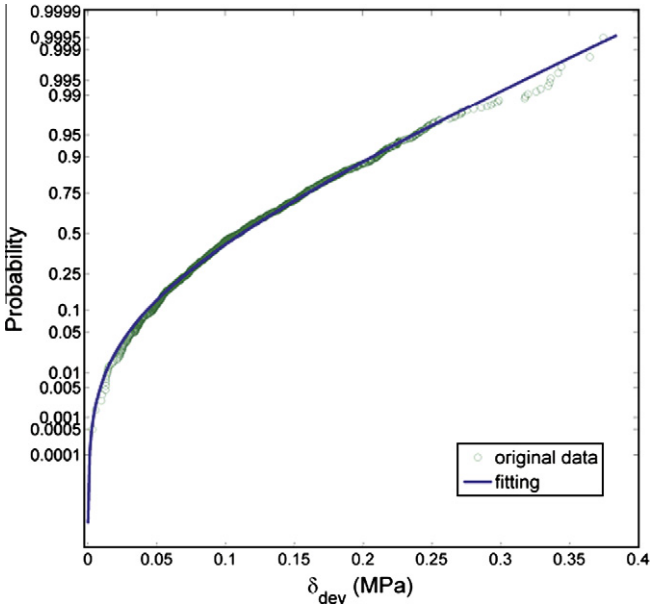

Fig. A.3. The probability plot of δ_{dev} and fitted Weibull distribution.

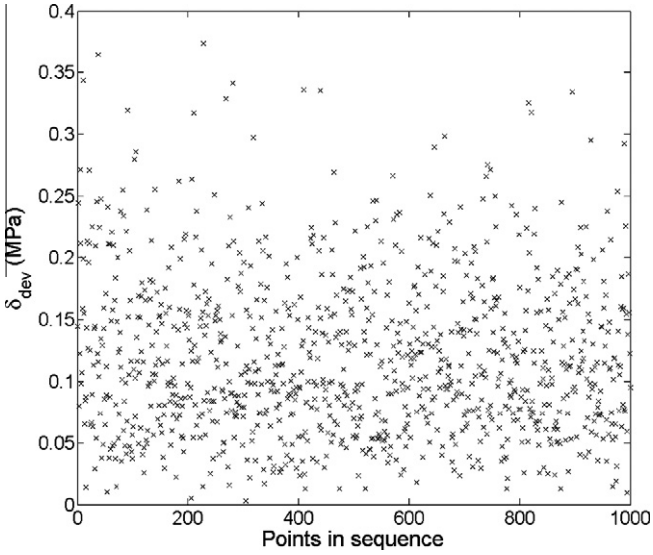

Fig. A.4. δ_{dev} of data points used for curve fitting.

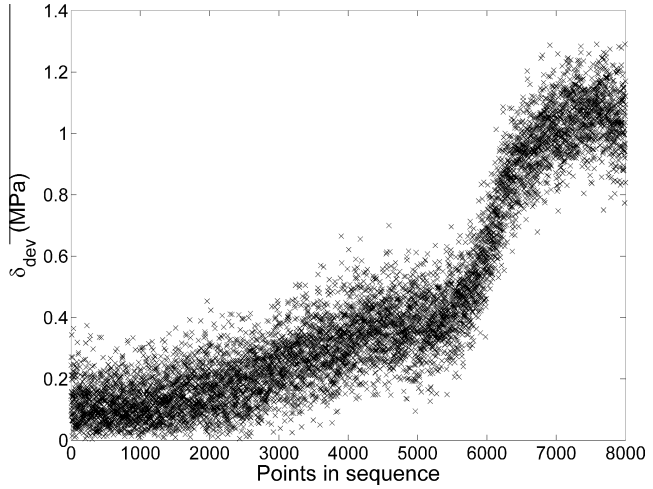

Fig. A.5. δ_{dev} of data points from the start to yielding.

The actual fitted parameters used in this probing were $d_{axial} = 0.1005$(MPa) and torsion = 0.091(MPa). These values of each probing are different since the scatter of data vary during the experiment. The values of two standard deviations were close; therefore the fitted result of δ_{dev} as a Weibull distribution was good with parameters $k = 1.9581$ and $\lambda = 0.1349$(MPa), shown in Fig. A.3. After finding out the parameters, $\delta_{est} = 0.292$(MPa) was chosen (99% cumulative probability). By plotting the data points for curve fitting directly, shown in Fig. A.4, it was seen that the range of variation was not large and did not increase rapidly. If plotting sequential points after the curve fitting, shown in Fig. A.5, an obvious increase appeared between point 6000 and point 7000. After the yield point had been decided within the range, the loading was stopped for a while before unloading so δ_{dev} did not increase after point 7000.

References

Boucher, M., Cayla, P., Cordebois, J.P., 1995. Experimental studies of yield surfaces of aluminum alloy and low carbon steel under complex biaxial loadings. Eur. J. Mech. A/Solids 14, 1–17.

Ellis, J.R., Robinson, D.N., Pugh, C.E., 1983. Time dependence in biaxial yield of type 316 stainless steel at room temperature. ASME J. Eng. Mater. Technol. 105, 250–256.

Hecker, S.S., 1971. Yield surfaces in prestrained aluminum and copper. Metall. Trans. 2, 2077–2086.

Helling, D.E., Miller, A.K., Stout, M.G., 1986. An experimental investigation of the yield Loci of 1100-O aluminum, 70:30 brass, and an overaged 2024 aluminum alloy after various prestrains. ASME J. Eng. Mater. Technol. 108, 313–320.

Ikegami, K., 1975a. A historical perspective of experimental study on subsequent yield surfaces for metals (part 1). J. Soc. Mat. Sci., Jpn. 24, 491–504.

Ikegami, K., 1975b. A historical perspective of experimental study on subsequent yield surfaces for metals (part 2). J. Soc. Mat. Sci., Jpn. 24, 709–719.

Ishikawa, H., 1997. Subsequent yield surface probed from its current center. Int. J. Plasticity 13, 533–549.

Kaneko, K., Ikegami, K., Shiratori, E., 1976. The yield condition and flow rule of a metal for the various pre-strain paths. Bull. JSME 19, 577–583.

Khan, A.S., Kazmi, R., Pandey, A., Stoughton, T., 2009. Evolution of subsequent yield surfaces and elastic constants with finite plastic deformation. Part-I: a very low work hardening aluminum alloy (Al6061 – T6511). Int. J. Plasticity 25, 1611–1625.

Khan, A.S., Pandey, A., Stoughton, T., 2010a. Evolution of subsequent yield surfaces and elastic constants with finite plastic deformation. Part-II: a very high work hardening aluminum alloy (annealed 1100 Al). Int. J. Plasticity 26, 1421–1431.

Khan, A.S., Pandey, A., Stoughton, T., 2010b. Evolution of subsequent yield surfaces and elastic constants with finite plastic deformation. Part-IIII: yield surface in tension–tension stress space (Al6061 – T6511 & annealed 1100 Al). Int. J. Plasticity 26, 1432–1441.

Kim, K.H., 1992. Evolution of anisotropy during twisting of cold drawn tubes. J. Mech. Phys. Solids 40, 127–139.

Kreissig, R., Schindler, J., 1986. Some experimental results on yield condition in plane stress state. Acta Mech. 65, 169–179.

Kumar, A., Samanta, S.K., Mallick, K., 1991. Study of the effect of deformation on the axes of anisotropy. ASME J. Eng. Mater. Technol. 113, 187–191.

Lipkin, J., Swearengen, J.C., 1975. On the subsequent yielding of an aluminum alloy following cyclic prestraining. Metall. Trans. A 6A, 167–177.

Lissenden, C.J., Lei, X., 2004. A more comprehensive method for yield locus construction for metallic alloys and composites. Exp. Mech. 44, 10–20.

Losilla, G., Tourabi, A., 2004. Hardening of a rolled sheet submitted to radial and complex biaxial tensile loadings. Int. J. Plasticity 20, 1789–1816.

Mallick, K., Samanta, S.K., Kumar, K., 1991. An experimental study of the evolution of yield loci for anisotropic materials subjected to finite shear deformation. ASME J. Eng. Mater. Technol. 113, 192–198.

Moreton, D.N., Moffat, D.G., Hornby, R.P., 1978. Techniques for investigating the yield surface behaviour of pressure-vessel materials. J. Strain Anal. 13, 185–191.

Ng, D.H.Y., Delich, M., Lee, L.H.N., 1979. Yielding of 6061-T6 aluminum tubings under dynamic biaxial loadings. Exp. Mech. 19, 200–206.

Phillips, A., Das, P.K., 1985. Yield surfaces and loading surfaces of aluminum and brass. Int. J. Plasticity 1, 89–109.

Phillips, A., Moon, H., 1977. An experimental investigation concerning yield surfaces and loading surfaces. Acta Mech. 27, 91–102.

Phillips, A., Tang, J.L., 1972. The effect of loading path on the yield surface at elevated temperatures. Int. J. Solids Struct. 8, 463.

Phillips, A., Tang, J.L., Ricciuti, M., 1974. Some new observations on yield surfaces. Acta Mech. 20, 23–39.

Shiratori, E., Ikegami, K., Kaneko, K., 1973. The influence of the Bauschinger effect on the subsequent yield condition. Bull. JSME 16, 1482–1493.

Shiratori, E., Ikegami, K., Kaneko, K., 1974. The stress vector and the subsequent yield surface in loading along the strain path with a corner. Bull. JSME 17, 1405–1412.

Stout, M.G., Martin, P.L., Helling, D.E., Canova, G.R., 1985. Multiaxial yield behavior of 1100 aluminum following various magnitudes of prestrains. Int. J. Plasticity 1, 163–174.

Takeda, T., 1991. The application of an anisotropic yield function of the sixth degree to orthotropic material. J. Strain Anal. 26, 201–207.

Takeda, T., 1993. Yield and flow behavior of initially anisotropic aluminum tube under multiaxial stresses. ASME J. Eng. Mater. Technol. 115, 77–82.

Takeda, T., Chen, Z., 2001. Off-axis torsion tests on tubular specimens of steel. ASME J. Eng. Mater. Technol. 123, 268–273.

Takeda, T., Mizukami, T., 2008. Plastic anisotropy of A2024BE-T6 and O aluminum alloys. J. Soc. Mat. Sci., Jpn. 57, 467–473.

Takeda, T., Nasu, Y., 1991. Evaluation of yield function including effects of third stress invariant and initial anisotropy. J. Strain Anal. 26, 47–53.

Williams, J.F., Svensson, N.L., 1971. Effect of torsional prestrain of the yield locus of 1100-F aluminium. J. Strain Anal. 6, 263–272.

Wu, H.C., 2003. Effect of loading-path on the evolution of yield surface for anisotropic metals subjected to large pre-strain. Int. J. Plasticity 19, 1773–1800.

Wu, H.C., 2005. Continuum Mechanics and Plasticity. Chapman & Hall/CRC Press, Boca Raton. pp. 323–398.

Wu, H.C., Yeh, W.C., 1991. On the experimental-determination of yield surfaces and some results of annealed 304 stainless-steel. Int. J. Plasticity 7, 803–826.